RNA-dependent RNA polymerase of predominant human norovirus forms liquid-liquid phase condensates as platforms for viral replication

Soni Kaundal[1], Ramakrishnan Anish [1], B. Vijayalakshmi Ayyar[2], Sreejesh Shanker[1], Gundeep Kaur[3], Sue E. Crawford[2], Jeroen Pollet[4], Fabio Stossi[5], Mary K. Estes[2,6], B.V. Venkataram Prasad[1,2]

[1]Department of Biochemistry and Molecular Pharmacology and [2]Department of Molecular Virology and Microbiology, Baylor College of Medicine, Houston, Texas, U.S.A. [3]Department of Epigenetics and Molecular Carcinogenesis, The University of Texas, MD Anderson Cancer Center, Houston, Texas U.S.A., [4]Department of Pediatrics-Tropical Medicine, [5]Department of Molecular and Cellular Biology, and [6]Department of Medicine, Baylor College of Medicine, Houston, Texas, U.S.A.

Corresponding author: B. V. Venkataram Prasad, E-mail: vprasad@bcm.edu

Abstract

Biomolecular condensates are membrane-less cellular foci formed via liquid-liquid-phase separation (LLPS) of specific biological macromolecules to provide specialized compartments for regulating cellular functions. Many viral proteins undergo LLPS to form such condensates to support viral replication and evade host antiviral responses, and thus these condensates are potential targets for designing antivirals. Human noroviruses (HuNoV) cause epidemic and sporadic gastroenteritis worldwide and are of significant health and economic burden. Here, we show that the RNA-dependent-RNA polymerase (RdRp) of the pandemic GII.4 HuNoV, which is essential for viral replication, forms distinct condensates capable of recruiting other viral replication components. Confocal microscopy and light scattering experiments show that RdRp phase separates into dynamic liquid-like condensates at physiological conditions. These condensates exhibit all the signature features of LLPS, including fluorescence recovery after photo-bleaching, droplet-fusion, surface wetting, and dripping. More importantly, within these condensates, the RdRp exhibits a significant time-dependent increase in its enzymatic activity and recruits other components, such as RNA and the viral genome-linked protein (VPg), which are essential for viral replication. Such condensates, recognized by anti-RdRp antibodies, are observed in HuNoV-infected human intestinal enteroid cultures. Together, our studies demonstrate a hitherto unsuspected activity of HuNoV RdRp to form LLPS, which we suggest provides distinct cellular sites for efficient viral replication and its regulation.

42 # Introduction

43 The compartmentalization of biomolecules is essential for efficiently regulating numerous
44 biological processes in a densely packed cellular environment. A wealth of new research has
45 shown that, apart from the traditional membrane-bound organelles, eukaryotic cells also contain
46 membrane-less organelles such as P granules, nucleoli, Cajal bodies, etc. [1-7]. These membrane-less
47 organelles, also known as biomolecular condensates, are formed by the process of liquid-liquid
48 phase separation (LLPS), where a single, uniform liquid phase separates into a dense phase that
49 coexists with the surrounding dilute phase [8-13]. These condensates, often initiated by a single
50 protein, selectively allow the incorporation of proteins and nucleic acids to provide exclusive
51 compartments for performing specialized cellular functions, including gene regulation, protein
52 synthesis, and signaling [13-15]. Depending upon the sequence and concentration of the protein, the
53 presence of other biomolecules, and the physiochemical properties of the surroundings, the dense
54 phase can have material properties of liquid, gel, or solid [2,3,16,17]. The liquid-like condensates
55 typically have a spherical shape with a dynamic interior, and exhibit the ability to fuse with each
56 other, deform upon physical contact, and revert to the spherical shape [2,3,9,10]. Signature features of
57 the proteins undergoing LLPS include the presence of a nucleic acid binding domain, a disordered
58 region, a low complexity region, and the ability to form oligomers [18-21]. The intrinsically
59 disordered regions drive LLPS by weak and dynamic intermolecular contacts, including
60 hydrophobic, electrostatic, hydrogen bonding, cation-π, and π-π interactions. The dynamic making
61 and breaking of these weak interactions give rise to the liquid-like nature of the phase separated
62 condensates [18,22,23]. The lack of a physical barrier and metastable state of these condensates allows
63 the rapid exchange of their components with surrounding molecules providing a unique
64 spatiotemporal regulation of macromolecular organization and cellular biochemistry [24,25].

65 Recent studies showed that several viral proteins can induce the formation of biomolecular
66 condensates via LLPS. These include, for example, NSP5 protein of rotavirus [26], N protein of
67 SARS-CoV2 [27], N protein of HIV-1 [28], and NS2 protein of bluetongue virus [29]. These condensates
68 are suggested to provide facile compartments also called viral factories or viroplasms for
69 concentrating the necessary components for efficient viral replication and assembly [30-32]. The
70 formation of condensates by LLPS is also proposed as a mechanism for evading the host antiviral
71 response [33,34].

72 Currently, it is unknown whether any of the proteins encoded by human norovirus
73 (HuNoV) undergoes LLPS to form biomolecular condensates. HuNoVs are the leading cause of
74 viral gastroenteritis and pose a significant global health and economic burden without any
75 approved vaccines or antivirals [35,36]. These icosahedral, single-stranded RNA viruses, belonging
76 to the *Norovirus* genus in the *Caliciviridae* family account for an estimated ~685 million cases and
77 ~212,000 deaths globally per year with an economic impact of $60 billion [35-39]. The NoVs are
78 classified into at least 10 genogroups (GI-GX) and 49 genotypes [40]. NoVs in genogroups GI, GII,
79 GIV, GVIII, and GIX infect humans [40,41], and among these, HuNoVs belonging to genogroup II
80 and genotype 4 (GII.4) are responsible for ~80 % of the outbreaks worldwide [42]. The NoV genome
81 is covalently linked to VPg and consists of three open reading frames (ORFs). ORF1 encodes a
82 polyprotein that is cleaved into six nonstructural proteins by the viral protease to produce p48
83 (NS1-2), p41 (NS3), p22 (NS4), VPg (NS5), protease (NS6), and RNA-dependent RNA
84 polymerase (RdRp) (NS7) [43]. The ORF2 and ORF3 encode the major capsid protein VP1 and a
85 minor structural protein VP2, respectively [44]. Our understanding of the HuNoV replication
86 processes in infected cells has been hampered by lack of a robust cell culture system. Much of our
87 current understanding of the entry and replication processes of HuNoVs have come from using the

88 human intestinal stem cell-derived, nontransformed enteroid (HIE) monolayer cultures for virus
89 cultivation [45-47].

90 Using bioinformatics analysis, we found that among the nonstructural proteins
91 encoded by the pandemic GII.4 Sydney strain, RdRp has the highest propensity to undergo LLPS
92 to form biomolecular condensates. In addition to the biophysical proprieties of GII.4 RdRp, such
93 as its modular architecture, the presence of an N-terminal disordered region, the ability to homo-
94 oligomerize and bind RNA, and the critical role it plays during viral replication prompted us to
95 experimentally test the hypothesis that GII.4 RdRp drives the formation of biomolecular
96 condensates that are conducive for viral replication through LLPS. Our studies show that RdRp,
97 consistent with its biophysical properties, indeed forms highly dynamic liquid-like condensates
98 via LLPS at physiologically relevant conditions and that the disordered N-terminal region of GII.4
99 RdRp is critical for LLPS. HuNoV infected HIEs cells show distinct condensates recognized by
100 RdRp antibodies. We also demonstrated a time-dependent increase of the GII.4 RdRp enzymatic
101 activity in the condensates and the ability of these condensates to sequester the components of
102 viral replication factories. Together these findings establish that HuNoV RdRp undergoes LLPS
103 to form biomolecular condensates, which can serve as platforms for viral replication.

104 # Results

105 **GII.4 RdRp exhibits the obligatory properties to undergo LLPS**

106 We used the DeePhase server [48] to analyze the primary amino acid sequences of all the
107 nonstructural proteins encoded by HuNoV GII.4 (Sydney) for their ability to undergo LLPS (**Fig.**
108 **1a**). This analysis predicted that RdRp, with an overall score of 0.67, has the highest propensity
109 to undergo LLPS. The known biochemical and enzymatic properties of RdRp are consistent with
110 this prediction. As a protein critical for the transcription and replication of genomic RNA, the

111 RNA binding property of RdRp satisfies one of the essential criteria for undergoing LLPS. Another
112 requirement is the presence of disordered regions. Analysis by PONDR (**Fig. 1b**) [49] and IUPred2
113 (**Fig. 1c**) [50] software shows the presence of disordered N- terminal ~50 residues in RdRp which is
114 consistent with the currently available crystal structures of NoV RdRps [51-54].

115 To experimentally confirm the LLPS driving properties of RdRp, such as the presence of
116 a disordered region, and the ability to form oligomers, we purified recombinantly expressed GII.4
117 RdRp and determined its X-ray crystal structure at 2.0 Å resolution using molecular replacement
118 (PDB ID: 8TUF). The crystal structure shows, as expected, all the features observed in the previous
119 crystallographic structures of the NoV RdRps [51-54], including the disordered N-terminal tail of 50
120 residues. The polypeptide fold resembles a partially closed right hand, with fingers, thumb, and
121 palm as subdomains (**Fig. 1d, Supplementary Table 1**). Size exclusion chromatography (SEC)
122 (**Fig. 1e**) and sedimentation velocity analytical ultracentrifugation (SV-AUC) (**Fig. 1f**) of the
123 recombinant RdRp show that while most of the RdRp (75 %) exists as a monomer in
124 physiologically relevant conditions, a fraction of which also tends to form dimers (15 %) and
125 higher-order oligomers. These experimental data, consistent with the bioinformatic predictions,
126 suggest that RdRp is a suitable candidate to investigate further its phase separation behavior.

127 **GII.4 RdRp undergoes phase separation to form dynamic liquid-like condensates**

128 To experimentally validate that RdRp undergoes LLPS, we studied its phase separation
129 behavior in vitro using light scattering experiments and confocal microscopy. Under physiological
130 conditions, homogeneously mixed RdRp (10 μM) phase separates to form a demixed turbid
131 solution when incubated at 37 °C for 45 min (**Fig. 2a**). The presence of condensates in the phase
132 separated solution was examined by confocal microscopy using a mixture of Atto 488-labeled (1
133 %) and unlabeled (99 %) RdRp. The micrographs showed the formation of spherical condensates
134 of micron diameter (**Fig. 2b**). We examined the liquid-like nature of these condensates by

135 assessing fluorescence recovery after photobleaching (FRAP) of the RdRp molecules. In this
136 experiment, the condensate was photo-bleached by intense laser light in a confocal microscope,
137 and then the fluorescence recovery of the photo-bleached area was monitored over time. The rapid
138 fluorescence recovery indicates diffusion of RdRp molecules. The FRAP data revealed a complete
139 fluorescence recovery (98 %) with a half-life ($t_{1/2}$) of 53.3 ± 2.1 s (**Fig. 2c, d**). Using time-lapse
140 confocal microscopy, we observed smaller GII.4 RdRp condensates fuse to form a larger
141 condensate (**Fig. 2e**). These condensates also undergo surface wetting and dripping (**Fig. 2f**). These
142 are also signature properties of liquid condensates. Our results clearly show that GII.4 RdRp
143 undergoes phase separation to form dynamic, liquid-like condensates, which are dense and high in
144 RdRp concentration yet allow the RdRp molecules to move freely within the condensates and
145 exchange with the surrounding environment.

146 **Molecular crowding, pH and salt concentration modulate phase separation properties of**
147 **GII.4 RdRp**

148 To examine whether there is a critical concentration of RdRp necessary to undergo LLPS,
149 and how this concentration is affected by molecular crowding agents such as polyethylene glycol
150 (PEG), typically used to simulate intracellular molecular crowding, we used two different
151 techniques: light scattering experiments to measure turbidity (**Fig. 3a**) and confocal microscopy to
152 assess LLPS formation (**Fig. 3d**). Different concentrations (0.5-25 μM) of GII.4 RdRp were
153 screened with and without PEG3350 (5-20 %). Confocal microscopy results suggest the critical
154 concentration for phase separation of GII.4 RdRp decreases from 5 μM to 0.5 μM by adding 10 %
155 PEG3350. The results show that increasing the molecular crowding, as expected inside the cells
156 during virus replication, decreases the critical concentration of the protein to phase separate. Our
157 light scattering experiments with PEG3350 also supported this result.

158 Considering the possibility, as observed in several recent studies [55,56,57,58], that changes in
159 intracellular pH and salt concentrations profoundly influence viral replication, we examined if
160 these factors affect the phase separation behavior of GII.4 RdRp. We observed increased turbidity
161 at an acidic pH of 5.5 compared to neutral pH, indicating that acidic pH promotes phase separation
162 more effectively than neutral pH. In contrast, the turbidity was significantly less at an alkaline pH
163 of 9.0 **(Fig. 3b)**. Since turbidity measurement is affected by the condensates size, shape, and
164 density, we further performed confocal microscopy at different pH conditions (**Fig. 3e**). RdRp
165 forms larger condensates at pH 5.5 than at pH 7.5 and, at pH 9, the condensates are few and have
166 an irregular shape. In addition, at pH 5.5, the critical concentration of RdRp required to form
167 LLPS decreased to 0.5 μM from 5 μM at pH 7.5. Since the predicted pI of GII.4 RdRp is 6.16,
168 these observations suggest that positive charges from basic residues in RdRp are critical for
169 promoting phase separation.

170 We also tested the effect of ionic strength on the phase separation of GII.4 RdRp by
171 measuring the turbidity of the solutions containing varying concentrations of NaCl using turbidity
172 measurements at 350 nm **(Fig. 3c),** and by imaging the condensates using confocal microscopy
173 **(Fig. 3f)**. These studies showed GII.4 RdRp undergoes phase separation at a NaCl concentration
174 as low as 10 mM, but not at concentrations >500 mM. The low ionic strength enhances protein-
175 protein electrostatic or π-π interactions, whereas high salt abolishes these interactions. Recent
176 studies have shown a similar behavior of the N protein of SARS-CoV-2 concerning pH and ionic
177 strength [28].

178 **The disordered N-terminal region is critical for GII.4 RdRp LLPS**

179 To validate the predicted role of the disordered N-terminal region of RdRp in forming the
180 condensates, we expressed and purified two N-terminal deletion constructs, GII.4 RdRp-NΔ13 and
181 GII.4 RdRp-NΔ51. Size exclusion chromatography of both deletion constructs shows a reduction

182 in their ability to form oligomers **(Fig. 4a)**. The CD spectra of both these constructs, showed two
183 distinct negative maxima at λ = 208 nm and 220 nm and a strong positive peak around 190 nm
184 indicative of an α-helical conformation and thus of proper folding of the deletion constructs **(Fig.**
185 **4b)**. Confocal microscopy images show that while GII.4 RdRp-NΔ13 can form liquid condensates
186 **(Fig. 4c)**, with a distorted and not spherical shape as compared with the full-length RdRp. The
187 distorted shape may be due to the weakened interactions resulting from the deletion of 13 residues,
188 which contain one aromatic residue. In contrast, deletion of N-terminal 51 residues (GII.4 RdRp-
189 NΔ51), which includes 5 aromatic residues, showed few and very small condensates that were
190 difficult to image. Our studies thus clearly demonstrate the flexible N-terminal region of GII.4
191 RdRp plays a critical role in its phase separation behavior.

192 **GII.4 infected HIE cells show phase separated RdRp condensates**

193 To investigate if RdRp condensate formation occurs in the context of viral replication, we
194 infected HIEs with GII.4 HuNoV and imaged the cells using confocal microscopy at different time
195 points post-infection. The confocal images show the presence of discrete and spherical condensates
196 of RdRp (detected by anti-RdRp antibody) **(Fig. 5a)**, which gradually increase in size over time.
197 We could not perform the FRAP/fusion experiments, in these virus-infected cells as these sample
198 needed to be fixed with paraformaldehyde and permeabilized for immunolabeling. In lieu of this,
199 we investigated if a recombinant GII.4 RdRp-eGFP forms condensates with liquid-like properties
200 upon transfection in HEK293T cells. Confocal microscopy imaging of the cells 24h post-
201 transfection showed round condensates formed by RdRp (**Fig. 5b)**. In contrast, cells expressing
202 eGFP alone, as a negative control, exhibit a diffuse distribution of eGFP (**Fig. 5b**). The condensates
203 formed by RdRp-eGFP show recovery after photo-bleaching indicating their liquid-like nature
204 **(Fig. 5b and c)**. Together, these findings provide supporting evidence that the observed
205 condensates in the virus-infected HIEs cells are formed via LLPS driven by RdRp.

206 **GII.4 RdRp is enzymatically active within liquid condensates**

207 Before investigating whether RdRp is active within the condensates, we used the
208 centrifugation method to estimate the concentration of phase separated RdRp, which was ~2.2
209 mM, ~200 times higher than the surrounding dilute phase, measured at A_{280}. To examine if the
210 highly concentrated protein in the condensate is enzymatically active, we monitored the formation
211 of dsRNA from a ssRNA template using a well-established fluorescence-based assay in which the
212 fluorescent dye SYTO9 binds specifically to dsRNA and fluoresces when excited at 485 nm **(Fig.**
213 **6a)**. We started the RNA polymerization reaction by adding rGTP (substrate) to a mixture which
214 includes RdRp (enzyme), polyC (ssRNA template), SYTO9 dye and other reaction components.
215 The reaction was performed in a 96 well glass bottom plate at 37 °C and imaged every 20 min
216 using a Yokogawa CV8000 high throughput spinning disk confocal microscope. Analysis of time-
217 lapse images shows an increase in fluorescence intensity within the condensates over time,
218 suggesting the formation of dsRNA **(Fig. 6b)**. An increase in the fluorescence intensity was
219 observed on the analysis of the total fluorescence intensity using CellPathfinder software **(Fig. 6c)**.
220 Together these results show concentration- and time-dependent increase in the enzymatic activity
221 of RdRp within the condensates.

222 **GII.4 RdRp LLPS recruits the critical components of viral replication machinery**

223 After demonstrating that RdRp can undergo LLPS to form enzymatically active
224 biomolecular condensates, we investigated whether these condensates could sequester the critical
225 components of the viral replication machinery, such as RNA and VPg, which functions as a primer
226 to initiate replication [59,60]. To examine the incorporation of RNA into the condensates, we mixed
227 equimolar amounts of Atto-488 RdRp andCy5 labeled RNA and imaged the samples using
228 confocal microscopy. Confocal microscopy revealed colocalization of Cy5-RNA and Atto 488-
229 RdRp condensates (**Fig. 7a**). Next, we tested if RdRp condensates can recruit GII.4 VPg. We

230 generated a reaction mixture by mixing equimolar amounts of Atto-488 RdRp and Atto-647N VPg
231 that were analyzed by confocal microscopy. We observed co-localization of VPg in the GII.4
232 RdRp condensates (**Fig. 7b**). The same results were obtained in HEK293T cells upon the
233 transfection of RdRp-eGFP and mCherry-VPg (**Fig. 7c**), where we could also observe the fusion
234 of these condensates (**Fig. 7d**). These results suggest that GII.4 RdRp phase separation offers a
235 mechanism for bringing together components of the viral replication machinery.

236 **Liquid to solid transition of GII.4 RdRp triggers the formation of amyloid-like fibrils.**

237 To study the dynamics of protein molecules during the maturation of the GII.4 RdRp
238 condensates, we monitored the material properties of the condensates for 24h using FRAP. In
239 initial experiments, the FRAP data revealed a complete fluorescence recovery (98 %) with a half-
240 life ($t_{1/2}$) of 53.3 ± 2.1 s, which decreased significantly with time (**Fig. 8a and b**). These
241 condensates retained liquid-like properties for about 4 h and then transformed into gel-like or solid-
242 like condensates. The increased rigidity and reduced dynamicity of protein molecules within the
243 condensates suggest that, over time, these condensates change from liquid-like to solid-like, likely
244 driven by the aggregation of proteins. Negative staining transmission electron microscopy of the
245 phase separated samples after 12 h of incubation at 37 °C showed fibrillar structures of varying
246 lengths **(Fig. 8c)**. Surprisingly, these fibrils have amyloid-like characteristics, such as binding to
247 amyloid-specific dyes thioflavin T (ThT) **(Fig. 8d)** and Congo red (CR) **(Fig. 8e)**. Such a
248 transformation from liquid-like to solid-like amyloid fibrils might provide a mechanism to regulate
249 viral replication.

250

251 # Discussion

252 In recent years, in addition to their demonstrated role in regulating various cellular
253 functions, biomolecular condensates formed via LLPS are strongly implicated in forming viral
254 replication factories/inclusion bodies [26,30,32]. For example, the viroplasms formed during rotavirus
255 infection, the sites for genome replication and sub-particle assembly, are considered biomolecular
256 condensates formed by the nonstructural proteins NSP5 and NSP2 [26]. In the case of SARS-CoV-
257 2, the N protein undergoes LLPS and sequesters components of the viral replication machinery [32].
258 Although replication factories (RFs) for HuNoVs are not yet characterized, murine NoVs form
259 distinct RFs [61]; however, the involvement of LLPS in these RFs is yet to be explored. In this
260 study, we show that RdRp of GII.4 HuNoV undergoes phase separation under physiologically
261 relevant conditions to create liquid-like, dynamic condensates that contain a protein-rich, dense,
262 and highly mobile environment. Our studies further suggest that distinct puncta observed in GII.4-
263 infected HIEs, which are recognized by anti-RdRp antibodies, are similar to the liquid-like
264 condensates formed by RdRp in HEK293T cells. We posit that these puncta are RdRp-initiated
265 liquid-like condensates representing RFs. Bioinformatics analysis shows that RdRps of almost all
266 the norovirus genogroups have a high propensity to form LLPS (**Supplementary Fig. 1**),
267 suggesting that LLPS formation by RdRp may be a common phenomenon in the Norovirus genera.
268 Although LLPS formed by cellular [62] and bacterial polymerases [63] is known, this is the first report
269 of a viral RdRp undergoing LLPS under physiological conditions both in vitro and in vivo.

270 **Unique aspects of HuNoV GII.4 RdRp induced LLPS – initiating a hub for viral replication**

271 Typically, cellular or viral proteins require additional client proteins, crowding agents, or
272 RNA to phase separate under physiological conditions [(35, 40)]. For example, up to 50 μM of the
273 SARS-CoV-2 N protein does not phase separate but adding 1 μM poly U significantly promotes
274 the phase separation [(40)]. Similarly, 35 μM NSP5 of rotavirus does not phase separate by itself; but
275 requires the presence of NSP2 or poly-arginine for phase separation [(35)]. In contrast, GII.4 RdRp

276 does not require any other viral protein or RNA to phase separate. It can phase separate at 5 μM
277 by itself and at 500 nM by adding a molecular crowding agent. Another observation, which may
278 have implications for viral replication, is that RdRp undergoes LLPS at pHs ranging from 5 to 9.
279 Interestingly, at pH 5, the critical concentration of RdRp to form LLPS is reduced from 5 μM to
280 500 nM. This is consistent with the previous observations that GII.4 and GII.3 HuNoVs infection
281 induces endosomal acidification [45,64]. The ability of GII.4 RdRp to readily form LLPS on its own
282 under various concentrations and conditions suggests that it likely plays a role in initiating the
283 formation of a sustainable platform for efficient viral replication during infection.

284 **RdRp condensates as viral replication factories**

285 A critical aspect of biomolecular condensates formed via LLPS, which is relevant for
286 forming viral RFs, is that they concentrate protein, nucleic acid, and other biomolecules to increase
287 and regulate reaction rates. In our studies, we observed not only that the concentration of phase
288 separated RdRp is ~200 times greater than that in the dilute phase but also that RdRp is
289 enzymatically active in such a crowded environment, supporting the hypothesis that these
290 condensates could be sites for viral replication. The observation that these RdRp condensates
291 promote the cooperative association/sequestering of other important viral components of the viral
292 replication machinery, such as RNA and VPg, further supports these condensates as platforms for
293 viral replication. VPg is a critical protein involved in viral replication and translation of viral
294 proteins. A recent study on murine NoV suggested that apart from its priming function, VPg can
295 physically interact with RdRp and enhance its polymerization activity [52]. Our results on HuNoV
296 RdRp also suggest that VPg increases the polymerization activity of RdRp (unpublished data).
297 Similarly, it is reported that the condensates formed by the N protein of SARS-CoV-2 can
298 sequester RNA and RdRp to provide a platform for viral replication [65].

299 Another protein that possibly is a component of the viral replication factory is p41 (NS3),
300 a membrane-anchored protein with RNA helicase activity [66]. p41 may be recruited into the RdRp
301 condensates containing VPg and RNA either by passive diffusion or by interacting with viral RNA.
302 Although not unequivocally demonstrated, earlier studies on picornaviruses, murine noroviruses,
303 and other positive sense RNA viruses have suggested that replication factories are associated with
304 membranes [61,67,68,69]. The formation of LLPS as a potential hub or a driving force for forming the
305 replication factories does not exclude the incorporation or association of membrane-anchored
306 proteins and lipids. Recent studies have implied such an association could reduce the critical
307 concentration for inducing LLPS and further for forming microdomains within the membrane-
308 associated condensates [70,71].

309 **Liquid to solid transition as a regulatory mechanism**

310 Another common phenomenon of biomolecular condensates is the transition from a liquid
311 to a solid state over time. The FRAP analysis of the GII.4 RdRp condensates over time shows a
312 lower diffusion rate of the RdRp molecules in the condensates. Consistent with this observation,
313 TEM imaging of the RdRp incubated at 37 °C overnight demonstrated the formation of fibrils.
314 Interestingly, these fibrils bind to amyloid-specific dyes such as ThT and CR, indicating the
315 amyloid-like nature of these fibrils. RdRps of several picornaviruses also form similar fibrillar
316 structures [72-74], although whether they exhibit amyloid-like properties is still unknown. The
317 transition from liquid to solid state leading to the formation of amyloid-like fibrils is plausibly a
318 mechanism for regulating replication. Another possibility is that these amyloid-like fibrils may
319 have a role in inducing cell toxicity, as shown in the case of amyloid-like fibrils formed by the
320 NS11 protein of SARS-CoV-2 [75].

321 In summary, our study reveals a previously unknown property of HuNoV RdRp in forming
322 biomolecular condensates. In addition to exhibiting all the properties for inducing the formation

323 of LLPS in vitro, we have shown that RdRp also readily undergoes LLPS in a cellular environment
324 that resembles the condensates observed in virus infected HIEs strongly implicating RdRp in
325 initiating and sustaining the viral RFs during HuNoV infection. Our bioinformatics analysis
326 suggests that this indeed may be a common phenomenon in most noroviruses. The implication of
327 RdRp in forming RFs also opens new targets for designing antivirals for HuNoV infections, which
328 remains a serious threat in children and immunocompromised patients.

329

330 # Material and methods

331 **Cloning, expression, and purification of proteins**

332 Codon optimized RdRp and VPg genes of HuNoV GII.4 Sydney strain (GenBank: AFV08794.1)
333 were synthesized and cloned in the pET28a vector for bacterial expression by Genscript U.S.A.
334 Inc with an N-terminal 6x His-tag to aid in the purification of both proteins. For mammalian
335 expression GII.4 RdRp was cloned in pcDNA3.1(+) vector with eGFP on C-terminal and GII.4
336 VPg was cloned in pcDNA3.1(+) vector with mCherry on N-terminal by Genscript U.S.A. Inc.
337 Two N-terminal truncations, i.e., GII.4 RdRp-NΔ13 and GII.4 RdRp-NΔ51 were also generated
338 by Genscript U.S.A. Inc. For the over-expression of proteins, the plasmids containing the desired
339 genes were transformed into *E coli* BL21 (DE3) cells. Protein expression was induced by addition
340 of 0.3 mM isopropyl β-D-1-thiogalactopyranoside at OD_{600} ~0.6. Cells were allowed to express
341 the protein at 18 °C for 16h with constant shaking at 200 rpm. Cells were harvested by
342 centrifugation at 4000xg for 30 min at 4 °C and the pellet was re-suspended in lysis buffer (20 mM
343 Tris-HCl pH 7.5, 250 mM NaCl, 5 mM imidazole and a cocktail of protease inhibitors) followed
344 by cell disruption using a microfluidizer. The supernatant was collected after centrifugation at
345 18,000xg for 45 min at 4 °C. The protein was purified by affinity chromatography using Ni-NTA

346 agarose (Qiagen) resin followed by gel filtration using Superdex 200 Increase 10/300 GL column
347 (G.E. Healthcare) in 20 mM Tris-HCl pH 7.5, 150 mM NaCl and 5 mM DTT. All the target
348 proteins GII.4 RdRp, GII.4 RdRp-NΔ13, GII.4 RdRp-NΔ51, and GII.4 VPg were purified using
349 the above-mentioned protocol to a purity of >95% as judged by SDS-PAGE and Coomassie blue
350 stain.

351 **Analytical Ultracentrifugation**

352 To study the oligomeric state of GII.4 RdRp, sedimentation velocity experiments of 10 μM GII.4
353 RdRp were carried out using a Beckman-Coulter XL-A analytical ultracentrifuge with a TiAn60
354 four hole rotor and two-channel epon centerpieces (12 mm) at 40,000 rpm at 22 °C. Absorbance
355 scans were recorded at 280 nm at 1 min intervals. A continuous distribution c(s) model was used
356 to fit multiple scans at regular intervals with SEDFIT [76]. The solvent density (ρ) and viscosity (η)
357 were calculated from the chemical composition of different proteins by SEDNTERP [77].

358 **Protein crystallization**

359 Crystallization screenings for GII.4 RdRp (10 mg/ml)was carried out by hanging-drop vapor
360 diffusion using the Mosquito crystallization robot (TTP LabTech) and imaged using Rock Imager
361 (Formulatrix) at 20 °C. The protein was crystallized under the condition 0.3 M Sodium Iodide, 0.1
362 M Sodium Acetate: HCl, pH 4.5 22.5 % (v/v) PurePEGs Cocktail. Crystals were flash-frozen
363 directly in liquid nitrogen.

364 **Structure determination and refinement**

365 Diffraction data for GII.4 RdRp was collected on APS BEAMLINE 17-ID. Diffraction data were
366 processed with IMOSFLM as implemented in the CCP4 suite [78]. The structure of NV RdRP (PDB
367 ID: 4LQ3) was used as a search model for molecular replacement (MR) using PHASER. The
368 atomic model including the side chain atoms was then subjected to iterative cycles of refinement

369 using PHENIX and further model building using COOT based on the difference maps [79,80]. Data
370 collection and refinement statistics following final refinement cycle are given in Table 1.

371 **Light scattering measurements**

372 Light scattering measurements of GII.4 RdRp were carried out on a FlexStation3 plate reader
373 (Molecular devices) using a 96-well flat bottom plate (Fisher Scientific) by measuring absorbance
374 at 350 nm at 37 °C at a regular interval of 2 min. Different concentrations of GII.4 RdRp (0.5, 1,
375 5, 10, 25 μM) were screened at varying concentrations of PEG3350 (0, 5, 10, 20%), pH (5.0, 6.0,
376 7.5, and 9.0) and salt (NaCl) (0, 150, 300, 500, and 750 mM).

377 **Fluorescence labeling of proteins**

378 For microscopic visualization of condensates, GII.4 RdRp, GII.4 RdRp-NΔ13 and GII.4 RdRp-
379 NΔ51were labeled with Atto-488 and GII.4 VPg was labeled with Atto-647N dye. For labeling an
380 Atto 488 protein labeling kit (Sigma-Aldrich, 38371) and an Atto 647N protein labeling kit
381 (Sigma-Aldrich, 76508) were used. The manufacture's provided protocol was used. Briefly, 8
382 mg/ml RdRp, RdRp-NΔ13, RdRp-NΔ51, and 6 mg/ml VPg were dialyzed in sodium bicarbonate
383 buffer solution, pH 9.5 (provided with kit). Then the protein solution was transferred to a vial
384 containing the reactive dye dissolved in 20 μl sodium bicarbonate buffer and incubated the reaction
385 mixture for 2 h at room temperature while gently stirring and protecting the vial from light. For
386 separation of protein-dye-conjugates from free dye, manufacturer's provided gel filtration columns
387 were used to achieve good separation of the protein-dye-conjugates from excess free dye (size
388 exclusion limit: 5 kDa). The protein-dye-conjugates were eluted in phosphate buffer, pH 7.5
389 provided with the kit.

390 **Confocal Microscopy**

391 Protein mixtures of 1% labeled and 99% unlabeled proteins were made at a concentration of 10
392 μM. An aliquot (15 μl) of the protein mixture was spotted onto 15 mm depression slides and

393 sandwiched with an 18 mm coverslip followed by sealing of the edges of the coverslip with
394 commercially available nail polish and allowed to phase separate at 37 °C for 45 min. The
395 condensates were visualized by Nikon A1R-s confocal microscope with 40X- air objective and 1
396 Airy unit aperture.

397 Different concentration of GII.4 RdRp (0.5, 1, 5, 10, 25 μM) were screened at varying
398 concentration of PEG3350 (0, 5, 10, 20 %), pH (5.0, 6.0, 7.5, and 9.0) and salt (NaCl) concentration
399 (0, 150, 300, 500, and 750 mM using Yokogawa CV8000 confocal imaging platform.

400 **Far-UV circular dichroism (CD) measurements**

401 Far-UV CD measurements of RdRp, RdRp-NΔ13, and RdRp-NΔ51 were carried out using
402 Circular Dichroism Spectroscopy (J-1500, Jasco), using a 1-mm path-length quartz cuvette. Data
403 were recorded using a final protein concentration of 8 μM proteins in 20 mM sodium phosphate
404 buffer pH 7.5. The spectra were averaged over three scans and were blank subtracted. The spectra
405 were then processed using Spectra Manager™ CDPro (Jasco) and plotted using Origin 2018.

406 **Negative stain transmission electron microscopy (EM)**

407 GII.4 RdRp (10 μM, 50 ul) was incubated at 37 °C at a constant shaking at 200 rpm for 20 s after
408 every 2 min for a period of 12 h. For preparing negatively stained grids, 3 μl of the GII.4 RdRp
409 (diluted 10 times) was adsorbed onto a glow discharged grid carbon-coated grid (CF200-CU;
410 EMS) for 60 s. The grid was blotted with Whatman's filter paper 541 and washed twice with
411 deionized water with intermittent blotting. The grid was further stained with three drops of 2 %
412 uranyl acetate with intermittent blotting to remove the residual stain. The grids were air-dried and
413 imaged at room temperature using a JEM 2100 transmission electron microscope operated at 200
414 keV (JEOL) equipped with a LaB6 filament, 3kx4k Direct Electron Detector (DE12) and a Gatan
415 4kx4k CCD at the cryo-EM core facility, Baylor college of Medicine. The images were recorded
416 at 15k using a low-dose procedure and a defocus range of −1 to −4 μm.

417 **GII.4 HuNoV infection of HIE monolayers**

418 Five day differentiated monolayers were infected with 1 x 10^7 GE of GII.4 stool filtrate in
419 CMGF(-) for 1 h at 37 ºC. After washing two times with CMGF(-), the HIEs were incubated at 37
420 °C for different time points (8-20 h). The cells were fixed with 4% paraformaldehyde (PFA) for
421 20 min at room temperature followed by permeabilization with 0.1% Triton X-100 (for
422 permeabilization) in PBS for 30 min at room temperature. The cells were incubated with 1:150
423 dilution of rabbit anti-RdRp [81] in 5 % BSA PBS at 4 °C overnight. The cells were washed three
424 times with PBS containing 0.1 % Triton X-100 and incubated with goat anti-rabbit 488 (#A-11008,
425 ThermoFisher Scientific) overnight at 4 º C to visualize the viral proteins. The cells were washed
426 three times, and the nuclei were stained with 4, 6-diamidino-2-phenylindole (DAPI) (300 nM)
427 followed by subsequent Z-stack images captured using a Nikon A1 confocal microscope.

428 **Mammalian cell line and expression**

429 HEK293T (ATCC, CRL-3216) (2 x 10^5 cells per well) were seeded in µ-Slide 8-well glass-bottom
430 plates (Ibidi) in DMEM media and incubated at 37 °C for 24 h. Cells were then transfected with
431 respective plasmids and incubated 37 °C. After 24 h, the cells were stained with Hoechst 33342
432 diluted in FluoroBRITE DMEM at a concentration of 1 mg/mL, incubated for 30 min at 37 °C.
433 These cells were further used for confocal microscopy and FRAP experiments.

434 **Fluorescence recovery after photobleaching (FRAP)**

435 FRAP studies were performed using a laser scanning confocal microscope (Nicon-A1R-s) with a
436 40x air objective. A circular area encompassing an entire condensate, was bleached with 404 nm
437 laser (100 %) for 20 iterations and recovery was recorded for 300 s at 10 s interval. For in vitro
438 FRAP study, 15 µl RdRp (10 µM) was spotted onto 15 mm depression slides and sandwiched with
439 18 mm coverslip followed by sealing of the edges of the coverslip with commercially available na

440 il polish and allowed to phase separate at 37 °C. After droplet formation was confirmed, the slides
441 containing the condensates were subjected to FRAP experiments at various time points as indicated
442 in the respective sections. For in cell FRAP, the bleaching of ROI was performed at 70 % laser
443 power for 20 iterations and recovery was recorded for 500 s at 15 s interval. The images were
444 corrected for laser bleaching by selecting a fluorescent region outside the ROI.

445 **Estimation of light phase and dense phase concentration**

446 The concentrations of dense phase and light phase were estimated using centrifugation by
447 following a previously described protocol [82]. For dense phase concentration estimation, 100 µl
448 RdRp (10 µM) was incubated at 37 °C for 45 min and centrifuged at ~ 25,000 x g at 37 °C for 15
449 min. After carefully removing the supernatant in several steps, the pure dense phase (~ 2 µL) was
450 re-suspended in 100 µl of the denaturation buffer (6M guanidine hydrochloride, 20 mM sodium
451 phosphate). The absorbance at 280 nm was recorded using nanodrop. The light phase concentration
452 was estimated from the absorbance of the supernatant at 280 nm.

453 **Fluorescence-based activity assay for GII.4 RdRp**

454 GII.4 RdRp activity was measured using a real-time fluorescence-based assay, which uses SYTO9,
455 a fluorescence dye that specifically binds dsRNA but not ssRNA template molecules. Reactions
456 were performed in individual wells of black 96-well flat-bottom plates (costar). The standard
457 reaction contained GII.4 RdRp (5 µM), 20 mM Tris-HCl pH 7.5, 5 mM MgCl2, 2.5 mM MnCl2,
458 40 µg/mL polyC, 5 U RNAseOUT (invitrogen) and 0.25 µM SYTO9 (Sigma-Aldrich). The
459 reaction was initiated by the addition of 300 µM GTP and the fluorescence was recorded after
460 every 2 min over 60 min at 30 °C using a plate reader FlexStation3 (Molecular devices). For
461 measuring the activity of RdRp in the condensates the same reaction was setup in 96 Well glass
462 bottom plates (Cellvis) and the fluorescence was recorded after every 4 min over 60 min at 30 °C
463 using the Yokogawa CV8000 confocal imaging platform.

464 **Thioflavin T fluorescence assays**

465 10 μM GII.4 RdRp was mixed with 10-fold molar excess of ThT and fluorescence intensity was
466 measured using excitation wavelength of 440 nm and emission wavelength of 482 nm using a plate
467 reader FlexStation3 (Molecular devices) at constant temperature of 37 °C and readings were
468 acquired every 2 min with continuous orbital shaking between reads over a period of 24 h. The top
469 of the each well was sealed using adhesive tape to minimize the rate of evaporation. Three
470 independent experiments were performed in triplicates and the bars represent the standard
471 deviation.

472 **Congo Red Binding Assay**

473 CR dye solution was prepared by mixing 7 mg/mL dye in and passed through 0.22 μm filter prior
474 to use. The spectrum of CR (5 μL in 1 mL 20 mM Tris-HCl pH 7.5, 150 mM NaCl and 5 mM
475 DTT) was recorded between 400 and 700 nm at room temperature (negative control). 10 μM RdRp
476 was incubated with C.R. for 12 h at 37 °C and the spectrum were recorded between 400 and 700
477 nm a plate reader FlexStation3 (Molecular devices)

478

479 **Acknowledgments**

480 This research used resources of the Advanced Photon Source, a U.S. Department of Energy (DOE)
481 Office of Science user facility operated for the DOE Office of Science by Argonne National
482 Laboratory under Contract No. DE-AC02-06CH11357. This work was supported by the NIH grant
483 P01 AI057788 and a grant (Q1279) from the Robert Welch Foundation (to BVVP). We also
484 acknowledge Integrated Microscopy Core and the CryoEM Core at Baylor College of Medicine
485 for all the microscopic experiments. We acknowledge the Protein Characterization Unit, Protein
486 and Monoclonal Antibody Production Core, BCM. GK was supported by the Cancer Prevention

and Research Institute of Texas grant RR160029 (to Xiaodong Cheng, MD Anderson Cancer Center).

References

1 Alberti, S. The wisdom of crowds: regulating cell function through condensed states of living matter. *J Cell Sci* **130**, 2789-2796 (2017). https://doi.org:10.1242/jcs.200295

2 Banani, S. F., Lee, H. O., Hyman, A. A. & Rosen, M. K. Biomolecular condensates: organizers of cellular biochemistry. *Nat Rev Mol Cell Biol* **18**, 285-298 (2017). https://doi.org:10.1038/nrm.2017.7

3 Boeynaems, S. *et al.* Protein Phase Separation: A New Phase in Cell Biology. *Trends Cell Biol* **28**, 420-435 (2018). https://doi.org:10.1016/j.tcb.2018.02.004

4 Fare, C. M., Villani, A., Drake, L. E. & Shorter, J. Higher-order organization of biomolecular condensates. *Open Biol* **11**, 210137 (2021). https://doi.org:10.1098/rsob.210137

5 Brangwynne, C. P. *et al.* Germline P granules are liquid droplets that localize by controlled dissolution/condensation. *Science* **324**, 1729-1732 (2009). https://doi.org:10.1126/science.1172046

6 Feric, M. *et al.* Coexisting Liquid Phases Underlie Nucleolar Subcompartments. *Cell* **165**, 1686-1697 (2016). https://doi.org:10.1016/j.cell.2016.04.047

7 Kaiser, T. E., Intine, R. V. & Dundr, M. De novo formation of a subnuclear body. *Science* **322**, 1713-1717 (2008). https://doi.org:10.1126/science.1165216

8 Alberti, S. & Dormann, D. Liquid-Liquid Phase Separation in Disease. *Annu Rev Genet* **53**, 171-194 (2019). https://doi.org:10.1146/annurev-genet-112618-043527

9 Alberti, S., Gladfelter, A. & Mittag, T. Considerations and Challenges in Studying Liquid-Liquid Phase Separation and Biomolecular Condensates. *Cell* **176**, 419-434 (2019). https://doi.org:10.1016/j.cell.2018.12.035

10 Alberti, S. & Hyman, A. A. Biomolecular condensates at the nexus of cellular stress, protein aggregation disease and ageing. *Nat Rev Mol Cell Biol* **22**, 196-213 (2021). https://doi.org:10.1038/s41580-020-00326-6

11 Fuxreiter, M. & Vendruscolo, M. Generic nature of the condensed states of proteins. *Nat Cell Biol* **23**, 587-594 (2021). https://doi.org:10.1038/s41556-021-00697-8

12 Hardenberg, M., Horvath, A., Ambrus, V., Fuxreiter, M. & Vendruscolo, M. Widespread occurrence of the droplet state of proteins in the human proteome. *Proc Natl Acad Sci U S A* **117**, 33254-33262 (2020). https://doi.org:10.1073/pnas.2007670117

13 Shin, Y. & Brangwynne, C. P. Liquid phase condensation in cell physiology and disease. *Science* **357** (2017). https://doi.org:10.1126/science.aaf4382

14 Peng, P. H., Hsu, K. W. & Wu, K. J. Liquid-liquid phase separation (LLPS) in cellular physiology and tumor biology. *Am J Cancer Res* **11**, 3766-3776 (2021).

15 Zhang, H. *et al.* Liquid-liquid phase separation in biology: mechanisms, physiological functions and human diseases. *Sci China Life Sci* **63**, 953-985 (2020). https://doi.org:10.1007/s11427-020-1702-x

528 16 Kroschwald, S. *et al.* Promiscuous interactions and protein disaggregases determine the
529 material state of stress-inducible RNP granules. *Elife* **4**, e06807 (2015).
530 https://doi.org:10.7554/eLife.06807
531 17 Jain, S. *et al.* ATPase-Modulated Stress Granules Contain a Diverse Proteome and
532 Substructure. *Cell* **164**, 487-498 (2016). https://doi.org:10.1016/j.cell.2015.12.038
533 18 Martin, E. W. & Mittag, T. Relationship of Sequence and Phase Separation in Protein Low-
534 Complexity Regions. *Biochemistry* **57**, 2478-2487 (2018).
535 https://doi.org:10.1021/acs.biochem.8b00008
536 19 Hughes, M. P. *et al.* Atomic structures of low-complexity protein segments reveal kinked
537 beta sheets that assemble networks. *Science* **359**, 698-701 (2018).
538 https://doi.org:10.1126/science.aan6398
539 20 Maharana, S. *et al.* RNA buffers the phase separation behavior of prion-like RNA binding
540 proteins. *Science* **360**, 918-921 (2018). https://doi.org:10.1126/science.aar7366
541 21 Pak, C. W. *et al.* Sequence Determinants of Intracellular Phase Separation by Complex
542 Coacervation of a Disordered Protein. *Mol Cell* **63**, 72-85 (2016).
543 https://doi.org:10.1016/j.molcel.2016.05.042
544 22 Choi, J. M., Holehouse, A. S. & Pappu, R. V. Physical Principles Underlying the Complex
545 Biology of Intracellular Phase Transitions. *Annu Rev Biophys* **49**, 107-133 (2020).
546 https://doi.org:10.1146/annurev-biophys-121219-081629
547 23 Uversky, V. N. Intrinsically disordered proteins in overcrowded milieu: Membrane-less
548 organelles, phase separation, and intrinsic disorder. *Curr Opin Struct Biol* **44**, 18-30 (2017).
549 https://doi.org:10.1016/j.sbi.2016.10.015
550 24 Hyman, A. A., Weber, C. A. & Julicher, F. Liquid-liquid phase separation in biology. *Annu*
551 *Rev Cell Dev Biol* **30**, 39-58 (2014). https://doi.org:10.1146/annurev-cellbio-100913-
552 013325
553 25 Wei, M. T. *et al.* Phase behaviour of disordered proteins underlying low density and high
554 permeability of liquid organelles. *Nat Chem* **9**, 1118-1125 (2017).
555 https://doi.org:10.1038/nchem.2803
556 26 Geiger, F. *et al.* Liquid-liquid phase separation underpins the formation of replication
557 factories in rotaviruses. *EMBO J* **40**, e107711 (2021).
558 https://doi.org:10.15252/embj.2021107711
559 27 Wang, J., Shi, C., Xu, Q. & Yin, H. SARS-CoV-2 nucleocapsid protein undergoes liquid-liquid
560 phase separation into stress granules through its N-terminal intrinsically disordered
561 region. *Cell Discov* **7**, 5 (2021). https://doi.org:10.1038/s41421-020-00240-3
562 28 Savastano, A., Ibanez de Opakua, A., Rankovic, M. & Zweckstetter, M. Nucleocapsid
563 protein of SARS-CoV-2 phase separates into RNA-rich polymerase-containing
564 condensates. *Nat Commun* **11**, 6041 (2020). https://doi.org:10.1038/s41467-020-19843-
565 1
566 29 Rahman, S. K., Ampah, K. K. & Roy, P. Role of NS2 specific RNA binding and
567 phosphorylation in liquid-liquid phase separation and virus assembly. *Nucleic Acids Res*
568 **50**, 11273-11284 (2022). https://doi.org:10.1093/nar/gkac904
569 30 Brocca, S., Grandori, R., Longhi, S. & Uversky, V. Liquid-Liquid Phase Separation by
570 Intrinsically Disordered Protein Regions of Viruses: Roles in Viral Life Cycle and Control of
571 Virus-Host Interactions. *Int J Mol Sci* **21** (2020). https://doi.org:10.3390/ijms21239045

572 31 Reddy, V. *et al.* Birnaviridae Virus Factories Show Features of Liquid-Liquid Phase
573 Separation and Are Distinct from Paracrystalline Arrays of Virions Observed by Electron
574 Microscopy. *J Virol* **96**, e0202421 (2022). https://doi.org:10.1128/jvi.02024-21
575 32 Chau, B. A., Chen, V., Cochrane, A. W., Parent, L. J. & Mouland, A. J. Liquid-liquid phase
576 separation of nucleocapsid proteins during SARS-CoV-2 and HIV-1 replication. *Cell Rep* **42**,
577 111968 (2022). https://doi.org:10.1016/j.celrep.2022.111968
578 33 Wang, S. *et al.* Targeting liquid-liquid phase separation of SARS-CoV-2 nucleocapsid
579 protein promotes innate antiviral immunity by elevating MAVS activity. *Nat Cell Biol* **23**,
580 718-732 (2021). https://doi.org:10.1038/s41556-021-00710-0
581 34 Wei, W. *et al.* When liquid-liquid phase separation meets viral infections. *Front Immunol*
582 **13**, 985622 (2022). https://doi.org:10.3389/fimmu.2022.985622
583 35 Kirk, M. D. *et al.* World Health Organization Estimates of the Global and Regional Disease
584 Burden of 22 Foodborne Bacterial, Protozoal, and Viral Diseases, 2010: A Data Synthesis.
585 *PLoS Med* **12**, e1001921 (2015). https://doi.org:10.1371/journal.pmed.1001921
586 36 Mortality, G. B. D. & Causes of Death, C. Global, regional, and national age-sex specific all-
587 cause and cause-specific mortality for 240 causes of death, 1990-2013: a systematic
588 analysis for the Global Burden of Disease Study 2013. *Lancet* **385**, 117-171 (2015).
589 https://doi.org:10.1016/S0140-6736(14)61682-2
590 37 Bartsch, S. M., Lopman, B. A., Ozawa, S., Hall, A. J. & Lee, B. Y. Global Economic Burden of
591 Norovirus Gastroenteritis. *PLoS One* **11**, e0151219 (2016).
592 https://doi.org:10.1371/journal.pone.0151219
593 38 Mattison, C. P., Cardemil, C. V. & Hall, A. J. Progress on norovirus vaccine research: public
594 health considerations and future directions. *Expert Rev Vaccines* **17**, 773-784 (2018).
595 https://doi.org:10.1080/14760584.2018.1510327
596 39 Lopman, B. A., Steele, D., Kirkwood, C. D. & Parashar, U. D. The Vast and Varied Global
597 Burden of Norovirus: Prospects for Prevention and Control. *PLoS Med* **13**, e1001999
598 (2016). https://doi.org:10.1371/journal.pmed.1001999
599 40 Chhabra, P. *et al.* Updated classification of norovirus genogroups and genotypes. *J Gen*
600 *Virol* **100**, 1393-1406 (2019). https://doi.org:10.1099/jgv.0.001318
601 41 van Beek, J. *et al.* Molecular surveillance of norovirus, 2005-16: an epidemiological
602 analysis of data collected from the NoroNet network. *Lancet Infect Dis* **18**, 545-553 (2018).
603 https://doi.org:10.1016/S1473-3099(18)30059-8
604 42 Yang, Y. *et al.* Genetic and phenotypic characterization of GII-4 noroviruses that circulated
605 during 1987 to 2008. *J Virol* **84**, 9595-9607 (2010). https://doi.org:10.1128/JVI.02614-09
606 43 Campillay-Veliz, C. P. *et al.* Human Norovirus Proteins: Implications in the Replicative
607 Cycle, Pathogenesis, and the Host Immune Response. *Front Immunol* **11**, 961 (2020).
608 https://doi.org:10.3389/fimmu.2020.00961
609 44 Vongpunsawad, S., Venkataram Prasad, B. V. & Estes, M. K. Norwalk Virus Minor Capsid
610 Protein VP2 Associates within the VP1 Shell Domain. *J Virol* **87**, 4818-4825 (2013).
611 https://doi.org:10.1128/JVI.03508-12
612 45 Ayyar, B. V. *et al.* CLIC and membrane wound repair pathways enable pandemic norovirus
613 entry and infection. *Nat Commun* **14**, 1148 (2023). https://doi.org:10.1038/s41467-023-
614 36398-z

615 46 Ettayebi, K. *et al.* Replication of human noroviruses in stem cell-derived human enteroids.
616 *Science* **353**, 1387-1393 (2016). https://doi.org:10.1126/science.aaf5211
617 47 Alvarado, G. *et al.* Broadly cross-reactive human antibodies that inhibit genogroup I and
618 II noroviruses. *Nat Commun* **12**, 4320 (2021). https://doi.org:10.1038/s41467-021-24649-
619 w
620 48 Saar, K. L. *et al.* Learning the molecular grammar of protein condensates from sequence
621 determinants and embeddings. *Proc Natl Acad Sci U S A* **118** (2021).
622 https://doi.org:10.1073/pnas.2019053118
623 49 Xue, B., Dunbrack, R. L., Williams, R. W., Dunker, A. K. & Uversky, V. N. PONDR-FIT: a meta-
624 predictor of intrinsically disordered amino acids. *Biochim Biophys Acta* **1804**, 996-1010
625 (2010). https://doi.org:10.1016/j.bbapap.2010.01.011
626 50 Dosztanyi, Z. Prediction of protein disorder based on IUPred. *Protein Sci* **27**, 331-340
627 (2018). https://doi.org:10.1002/pro.3334
628 51 Deval, J., Jin, Z., Chuang, Y. C. & Kao, C. C. Structure(s), function(s), and inhibition of the
629 RNA-dependent RNA polymerase of noroviruses. *Virus Res* **234**, 21-33 (2017).
630 https://doi.org:10.1016/j.virusres.2016.12.018
631 52 Lee, J. H. *et al.* Insight Into the Interaction Between RNA Polymerase and VPg for Murine
632 Norovirus Replication. *Front Microbiol* **9**, 1466 (2018).
633 https://doi.org:10.3389/fmicb.2018.01466
634 53 Shaik, M. M., Bhattacharjee, N., Feliks, M., Ng, K. K. & Field, M. J. Norovirus RNA-
635 dependent RNA polymerase: A computational study of metal-binding preferences.
636 *Proteins* **85**, 1435-1445 (2017). https://doi.org:10.1002/prot.25304
637 54 Smertina, E., Urakova, N., Strive, T. & Frese, M. Calicivirus RNA-Dependent RNA
638 Polymerases: Evolution, Structure, Protein Dynamics, and Function. *Front Microbiol* **10**,
639 1280 (2019). https://doi.org:10.3389/fmicb.2019.01280
640 55 Batishchev, O. V. *et al.* pH-Dependent Formation and Disintegration of the Influenza A
641 Virus Protein Scaffold To Provide Tension for Membrane Fusion. *J Virol* **90**, 575-585
642 (2016). https://doi.org:10.1128/JVI.01539-15
643 56 Liu, H., Maruyama, H., Masuda, T., Honda, A. & Arai, F. The Influence of Virus Infection on
644 the Extracellular pH of the Host Cell Detected on Cell Membrane. *Front Microbiol* **7**, 1127
645 (2016). https://doi.org:10.3389/fmicb.2016.01127
646 57 Jimenez, L. *et al.* Acid pH Increases SARS-CoV-2 Infection and the Risk of Death by COVID-
647 19. *Front Med (Lausanne)* **8**, 637885 (2021). https://doi.org:10.3389/fmed.2021.637885
648 58 Kreutzberger, A. J. B. *et al.* SARS-CoV-2 requires acidic pH to infect cells. *Proc Natl Acad*
649 *Sci U S A* **119**, e2209514119 (2022). https://doi.org:10.1073/pnas.2209514119
650 59 Rohayem, J., Robel, I., Jager, K., Scheffler, U. & Rudolph, W. Protein-primed and de novo
651 initiation of RNA synthesis by norovirus 3Dpol. *J Virol* **80**, 7060-7069 (2006).
652 https://doi.org:10.1128/JVI.02195-05
653 60 Belliot, G., Sosnovtsev, S. V., Chang, K. O., McPhie, P. & Green, K. Y. Nucleotidylylation of
654 the VPg protein of a human norovirus by its proteinase-polymerase precursor protein.
655 *Virology* **374**, 33-49 (2008). https://doi.org:10.1016/j.virol.2007.12.028
656 61 Hyde, J. L. *et al.* Mouse norovirus replication is associated with virus-induced vesicle
657 clusters originating from membranes derived from the secretory pathway. *J Virol* **83**,
658 9709-9719 (2009). https://doi.org:10.1128/JVI.00600-09

659 62 Palacio, M. & Taatjes, D. J. Merging Established Mechanisms with New Insights:
660 Condensates, Hubs, and the Regulation of RNA Polymerase II Transcription. *J Mol Biol* **434**,
661 167216 (2022). https://doi.org:10.1016/j.jmb.2021.167216
662 63 Ladouceur, A. M. *et al.* Clusters of bacterial RNA polymerase are biomolecular
663 condensates that assemble through liquid-liquid phase separation. *Proc Natl Acad Sci U S*
664 *A* **117**, 18540-18549 (2020). https://doi.org:10.1073/pnas.2005019117
665 64 Murakami, K. *et al.* Bile acids and ceramide overcome the entry restriction for GII.3 human
666 norovirus replication in human intestinal enteroids. *Proc Natl Acad Sci U S A* **117**, 1700-
667 1710 (2020). https://doi.org:10.1073/pnas.1910138117
668 65 Perdikari, T. M. *et al.* SARS-CoV-2 nucleocapsid protein undergoes liquid-liquid phase
669 separation stimulated by RNA and partitions into phases of human ribonucleoproteins.
670 *bioRxiv* (2020). https://doi.org:10.1101/2020.06.09.141101
671 66 Li, T. F. *et al.* Human Norovirus NS3 Has RNA Helicase and Chaperoning Activities. *J Virol*
672 **92** (2018). https://doi.org:10.1128/JVI.01606-17
673 67 Harak, C. & Lohmann, V. Ultrastructure of the replication sites of positive-strand RNA
674 viruses. *Virology* **479-480**, 418-433 (2015). https://doi.org:10.1016/j.virol.2015.02.029
675 68 Zhang, Y., Cao, X. & Li, D. Architecture of viral replication factories. *Oncotarget* **6**, 30439-
676 30440 (2015). https://doi.org:10.18632/oncotarget.5900
677 69 Zhang, Z. *et al.* Host Lipids in Positive-Strand RNA Virus Genome Replication. *Front*
678 *Microbiol* **10**, 286 (2019). https://doi.org:10.3389/fmicb.2019.00286
679 70 Ditlev, J. A. Membrane-associated phase separation: organization and function emerge
680 from a two-dimensional milieu. *J Mol Cell Biol* **13**, 319-324 (2021).
681 https://doi.org:10.1093/jmcb/mjab010
682 71 Miller, E. J. *et al.* Divide and conquer: How phase separation contributes to lateral
683 transport and organization of membrane proteins and lipids. *Chem Phys Lipids* **233**,
684 104985 (2020). https://doi.org:10.1016/j.chemphyslip.2020.104985
685 72 Lyle, J. M., Bullitt, E., Bienz, K. & Kirkegaard, K. Visualization and functional analysis of
686 RNA-dependent RNA polymerase lattices. *Science* **296**, 2218-2222 (2002).
687 https://doi.org:10.1126/science.1070585
688 73 Bentham, M., Holmes, K., Forrest, S., Rowlands, D. J. & Stonehouse, N. J. Formation of
689 higher-order foot-and-mouth disease virus 3D(pol) complexes is dependent on elongation
690 activity. *J Virol* **86**, 2371-2374 (2012). https://doi.org:10.1128/JVI.05696-11
691 74 Loundras, E. A. *et al.* Higher-order structures of the foot-and-mouth disease virus RNA-
692 dependent RNA polymerase required for genome replication. *Commun Biol* **5**, 61 (2022).
693 https://doi.org:10.1038/s42003-021-02989-z
694 75 Bhardwaj, T. *et al.* Amyloidogenic proteins in the SARS-CoV and SARS-CoV-2 proteomes.
695 *Nat Commun* **14**, 945 (2023). https://doi.org:10.1038/s41467-023-36234-4
696 76 Schuck, P., Perugini, M. A., Gonzales, N. R., Howlett, G. J. & Schubert, D. Size-distribution
697 analysis of proteins by analytical ultracentrifugation: strategies and application to model
698 systems. *Biophys J* **82**, 1096-1111 (2002). https://doi.org:10.1016/S0006-3495(02)75469-
699 6
700 77 Laue TM, S. B., Ridgeway TM., Pelletier SL. Computer-aided Interpretation of
701 Sedimentation Data for Proteins. *Analytical ultracentrifugation in biochemistry and*
702 *polymer science*, pp. 90–25 (1992).

703 78 Winn, M. D. *et al.* Overview of the CCP4 suite and current developments. *Acta Crystallogr*
704 *D Biol Crystallogr* **67**, 235-242 (2011). https://doi.org:10.1107/S0907444910045749
705 79 Adams, P. D. *et al.* PHENIX: a comprehensive Python-based system for macromolecular
706 structure solution. *Acta Crystallogr D Biol Crystallogr* **66**, 213-221 (2010).
707 https://doi.org:10.1107/S0907444909052925
708 80 Emsley, P., Lohkamp, B., Scott, W. G. & Cowtan, K. Features and development of Coot.
709 *Acta Crystallogr D Biol Crystallogr* **66**, 486-501 (2010).
710 https://doi.org:10.1107/S0907444910007493
711 81 Karandikar, U. C. *et al.* Detection of human norovirus in intestinal biopsies from
712 immunocompromised transplant patients. *J Gen Virol* **97**, 2291-2300 (2016).
713 https://doi.org:10.1099/jgv.0.000545
714 82 Milkovic, N. M. & Mittag, T. Determination of Protein Phase Diagrams by Centrifugation.
715 *Methods Mol Biol* **2141**, 685-702 (2020). https://doi.org:10.1007/978-1-0716-0524-0_35
716

717

718 **Figures and legends**

719
720

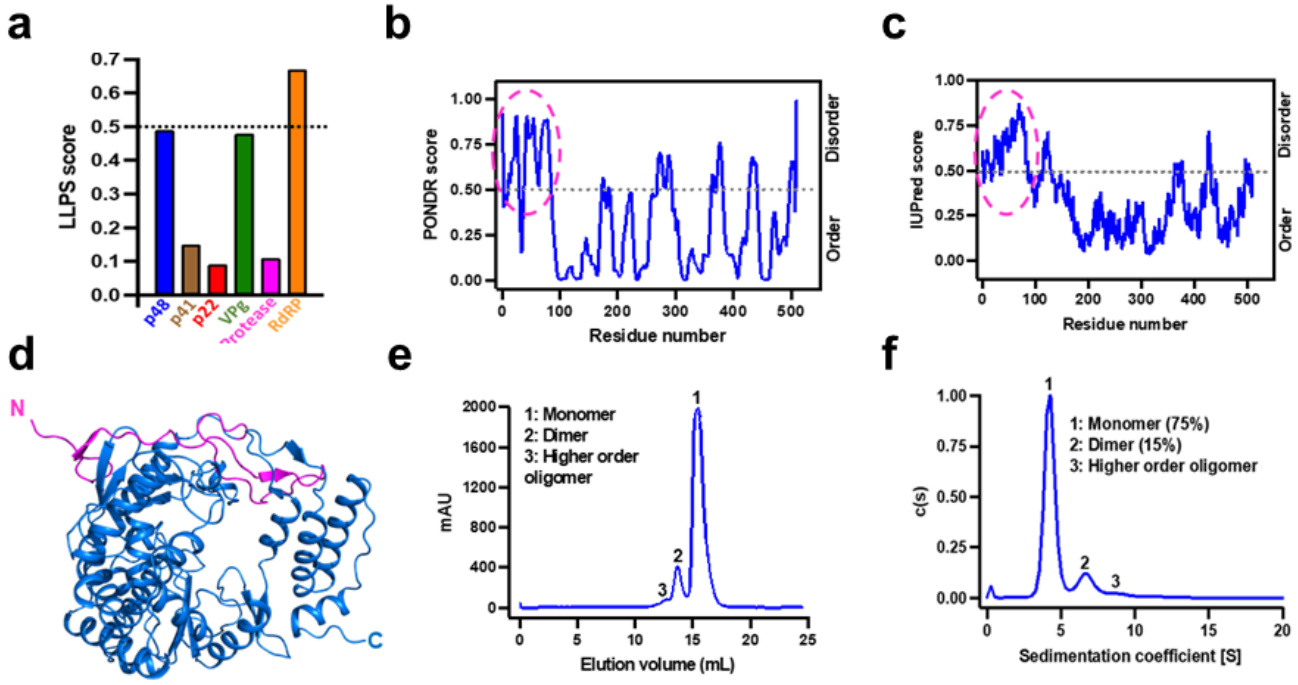

721
722

723

724 **Figure 1. GII.4 RdRp has the required properties to undergo LLPS**. **(a)** Bioinformatics
725 analysis of the primary amino acid sequences of all nonstructural proteins of HuNoV GII.4 to
726 predict LLPS propensity using DeePhase. The dotted black line indicates the threshold LLPS score
727 of proteins to undergo LLPS. **(b-c)** The disorder prediction of GII.4 RdRp primary amino acid
728 sequence using bioinformatics tools **(b)** PONDR **(c)** IUPred2. The dotted black line in both the
729 panels indicates the threshold disorder score. The dotted pink circle in both the panels shows the
730 predicted disordered N-terminal region. (**d)** The cartoon representation of the crystal structure of
731 GII.4 RdRp showing the disordered N-terminal region colored in pink. **(e-f)** The oligomeric state
732 of GII.4 RdRp analyzed using **(e)** size exclusion chromatography and **(f)** sedimentation velocity
733 analytical ultracentrifugation.

734

735

736

737

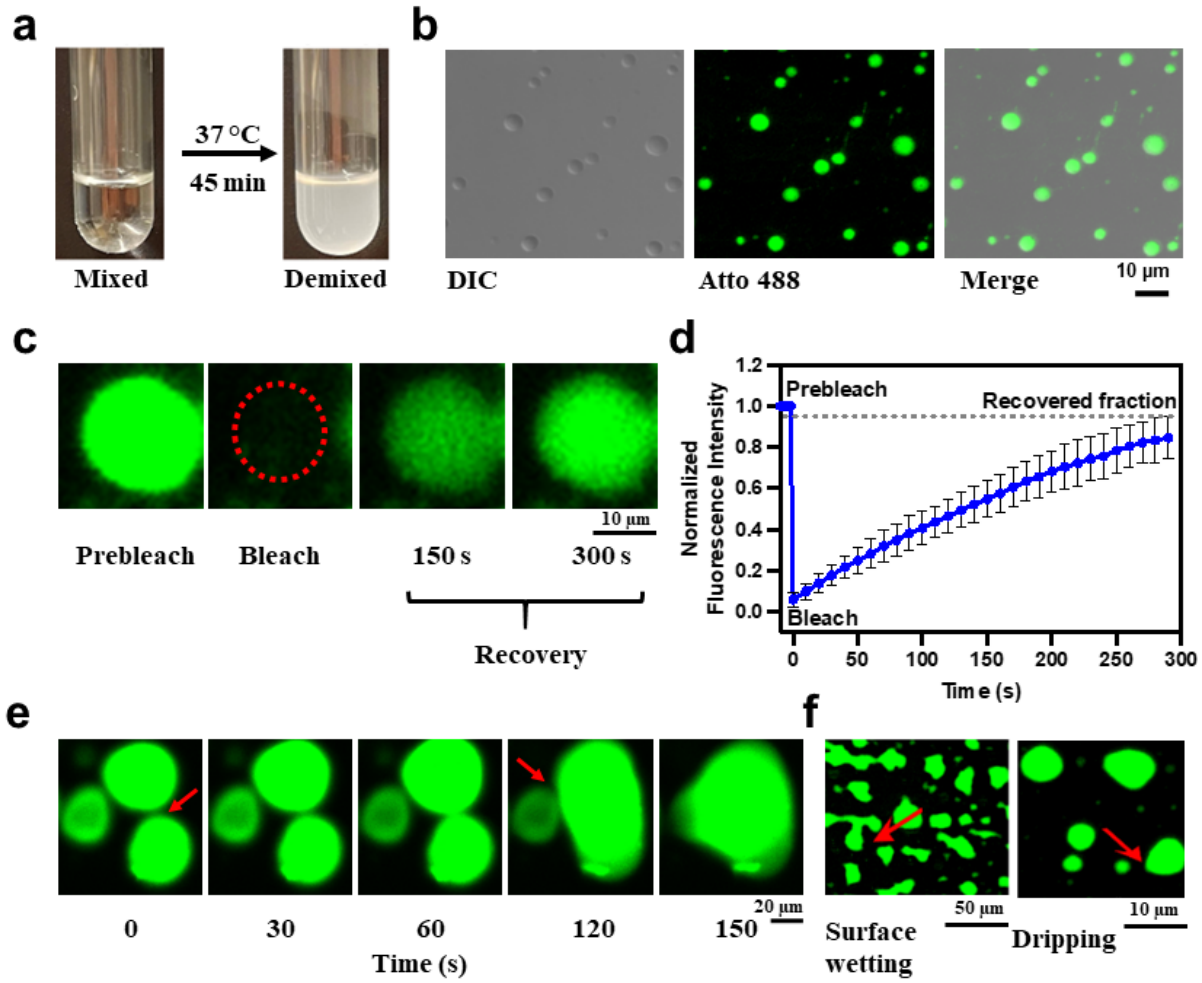

Figure 2. GII.4 RdRp undergoes LLPS in vitro. (a) Phase separation of RdRp from a homogeneous mixed-phase into a demixed phase upon incubation at 37 °C for 45 min. **(b)** Differential interference contrast (DIC) and confocal images of phase separated RdRp (1 % Atto 488 labeled and 99 % unlabeled). Phase separated GII.4 RdRp possesses liquid-like properties. **(c)** FRAP of RdRp in condensate photobleached at the position indicated by the red circle. **(d)** The graph shows the recovery curve where normalized fluorescence intensity was plotted against time. **(e)** Time-lapse images of RdRp condensates exhibits formation of larger condensate by fusion of smaller condensates over time. The red arrows indicate the site of fusion. **(f)** Surface wetting and dripping using confocal microscopy. The red arrows indicate the position of surface wetting and dripping.

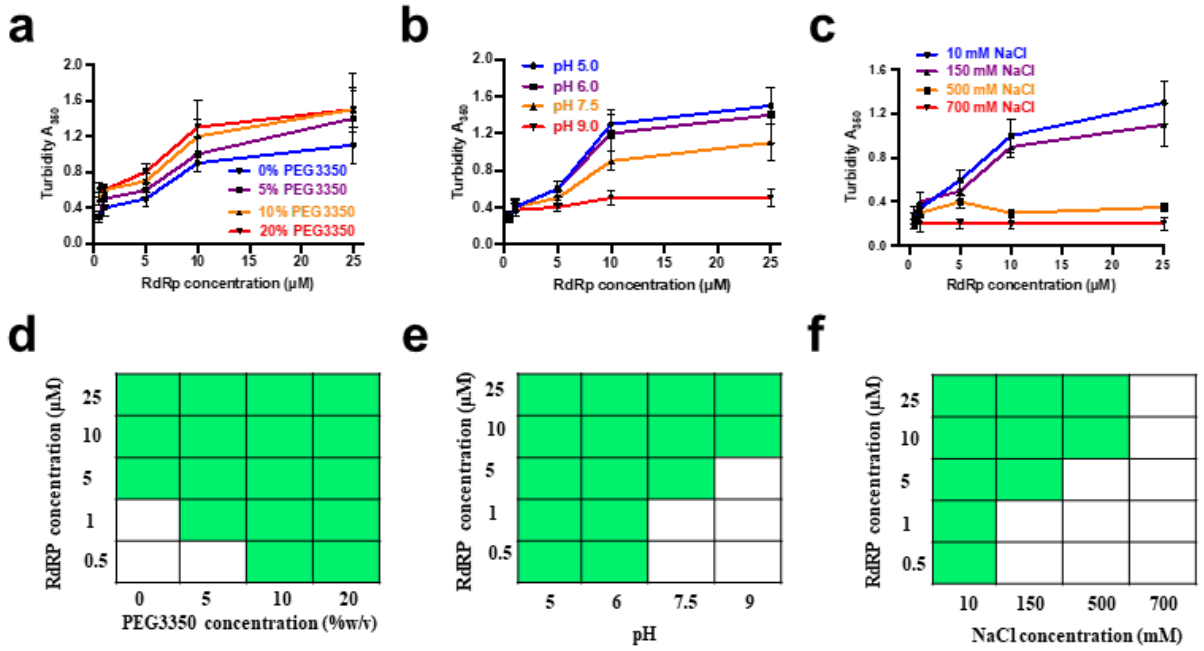

Figure 3. Phase separation of GII.4 RdRp is modulated by PEG3350 concentration, pH, and salt concentration. Effect of **(a)** protein and PEG3350 concentrations, **(b)** protein concentrations and pH, **(c)** protein and salt concentrations on the phase separation of RdRp was assessed by measuring the turbidity of the samples at OD 350 nm. **(d-f)** A phase diagram of RdRp at **(d)** protein and PEG3350 concentrations, **(e)** at protein concentrations and pH, at **(f)** protein and salt concentrations constructed from the confocal microscopy images. The green boxes indicate LLPS (condensate state) and white boxes indicate no LLPS (soluble state).

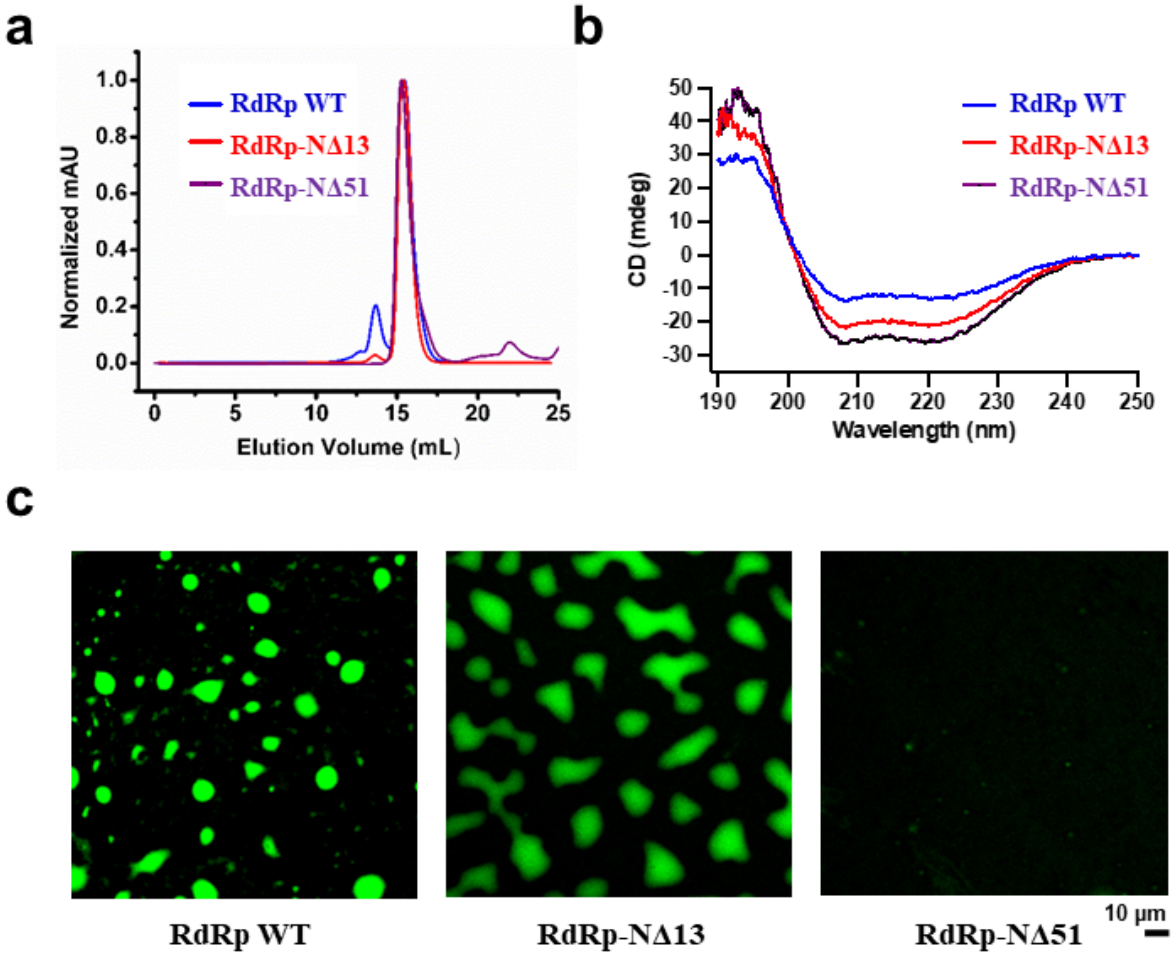

Figure 4. Effect of N-terminal deletion on phase separation of GII.4 RdRp. RdRp WT, RdRp-NΔ13, and RdRp-NΔ51 were analyzed by **(a)** The size exclusion chromatography profile **(b)** CD spectroscopy profile and **(c)** confocal microscopy.

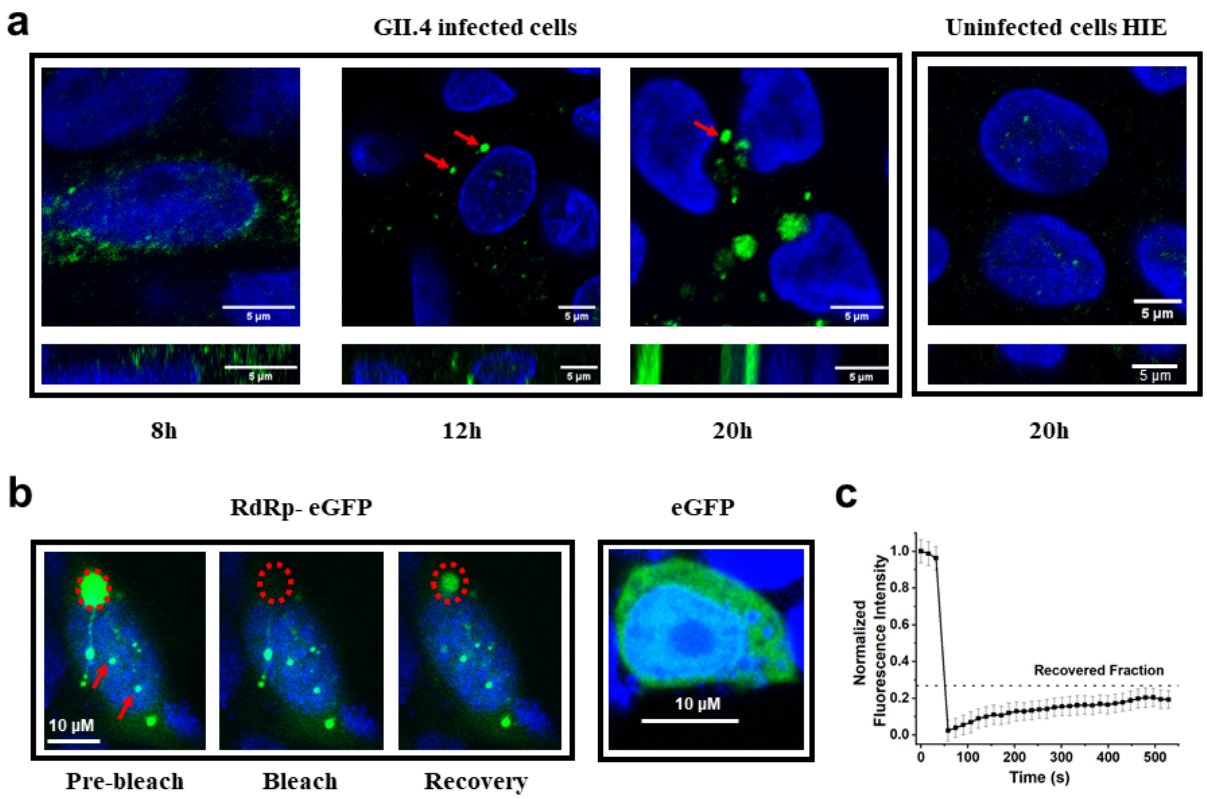

Figure 5. RdRp forms condensates in GII.4 infected HIEs. (a) Confocal microscopy images of GII.4 HuNoV-infected HIEs at different time points post infection showing condensate formation detected by anti-RdRp antibody (green). Uninfected HIEs were used as negative control. Red arrows indicate the position of representative condensates. **(b)** Transfection of RdRp-eGFP in HEK293T cells showing condensate formation (red arrows). FRAP experiment was performed on one of the condensates (marked by red circle) which shows recovery of the RdRp molecules. The eGFP transfected HEK293T cells were used as a negative control where GFP is diffuse. **(c)** Recovery curve of normalized fluorescence intensity was plotted against time for FRAP experiment.

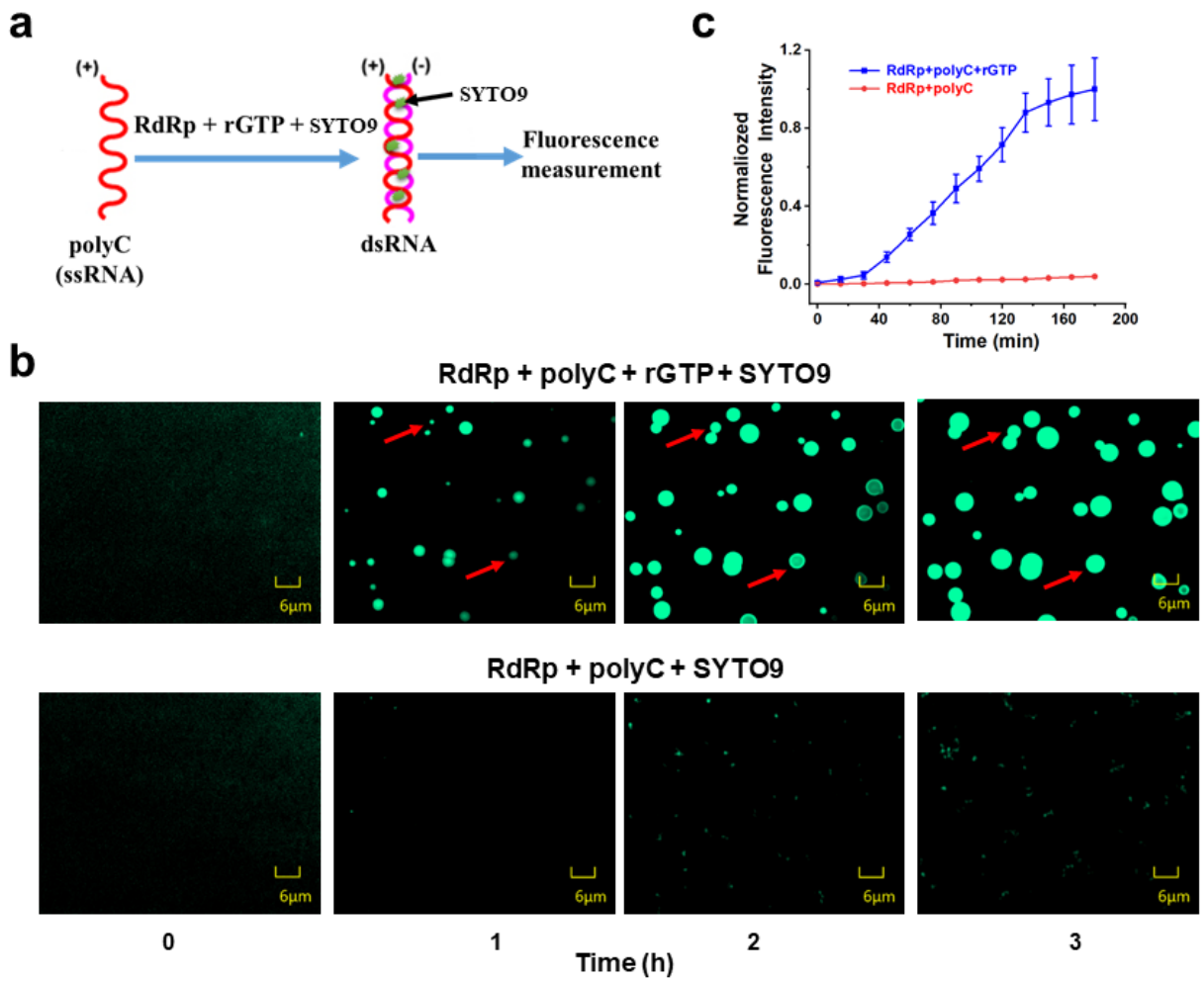

Figure 6. GII.4 RdRp is enzymatically active in the condensates. (a) A schematic representation of the assay to detect the formation of dsRNA from ssRNA by RdRp using SYTO9 dye. **(b)** Microscopic images of time-dependent activity of RdRp measured by fluorescence intensity of SYTO9: the upper panel contains all the components of reaction mixture. A time-dependent increase in the fluorescence intensity of SYTO9 which is an indicative of dsRNA formation within the condensates was observed. The red arrows indicate representative condensates showing an increase in fluorescence intensity over time. The lower panel without rGTP in reaction mixture serves as a negative control. **(c)** The graph of normalized fluorescence intensity plotted against time shows an overall increase in fluorescence intensity.

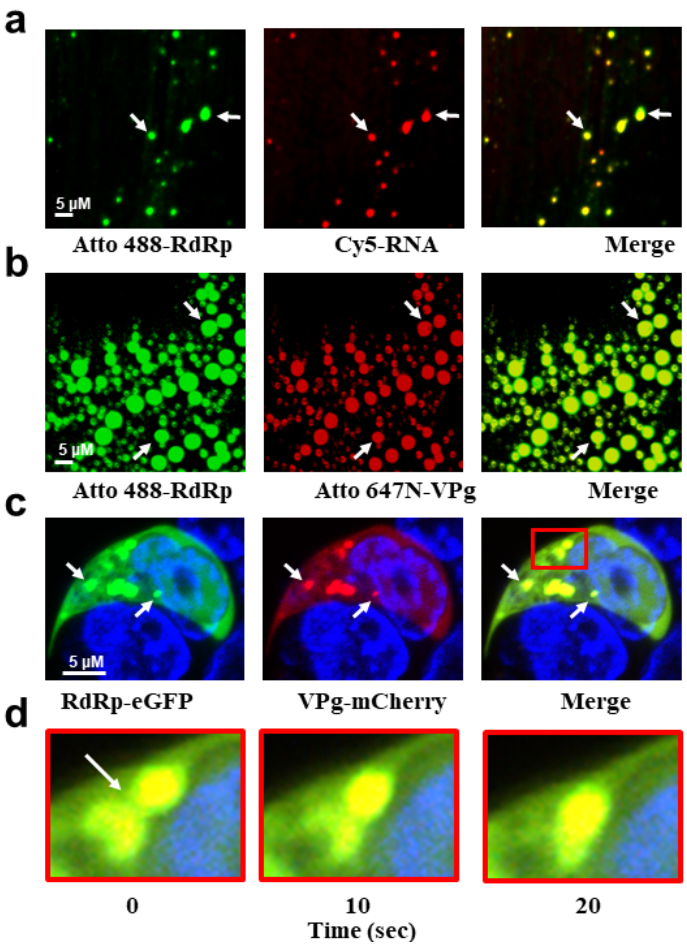

Figure 7. GII.4 RdRp condensates sequester components of viral replication machinery Confocal images showing the recruitment of **(a)** Cy5-RNA and **(b)** Atto 647N-VPg into the spherical condensates formed by Atto 488-RdRp. **(c)** Colocalization (yellow) of mCherry-VPg (red) and GII.4 RdRp-eGFP (green) was seen on overexpression of these protein in HEK293T cells. In the above panels, the white arrows indicate the position of representative condensates and their co-localization with the components of replication machinery. **(d)** Time lapse images of site indicated by red box in panel C showing the fusion of condensates. The white arrow indicates the position of fusion.

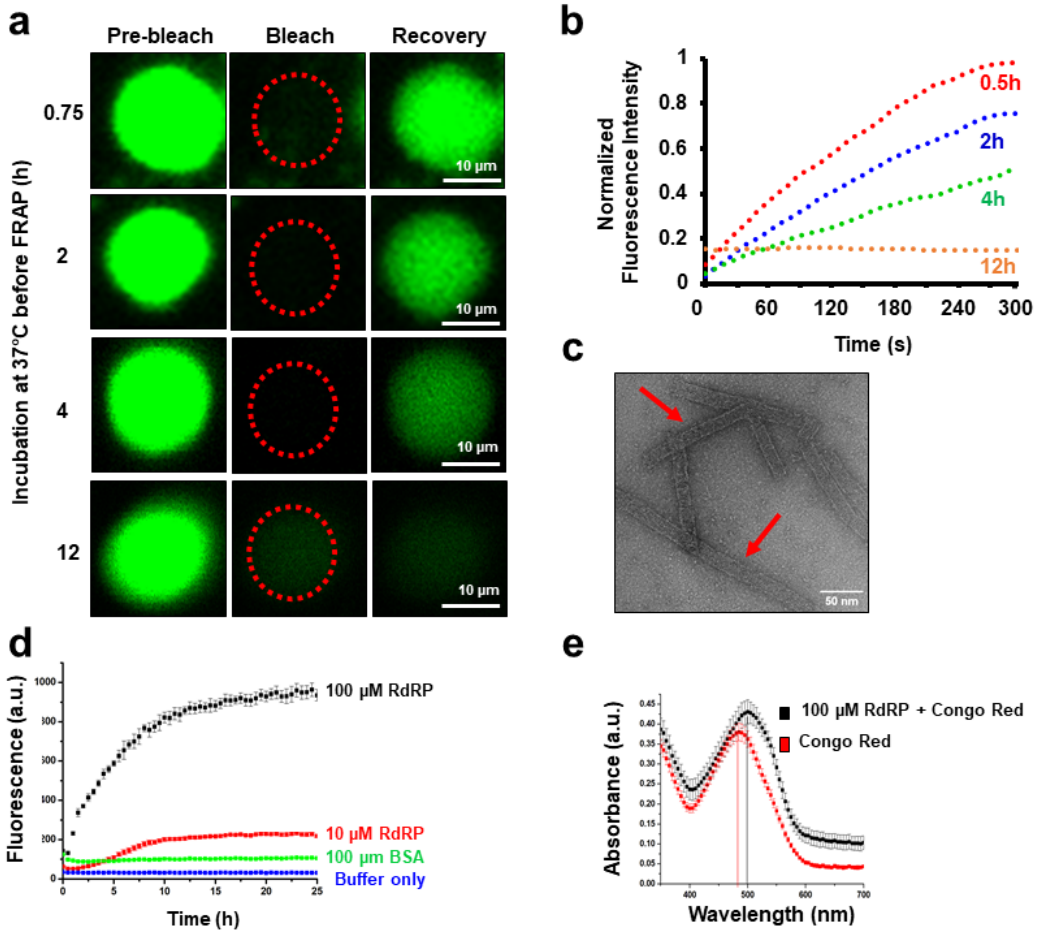

Figure 8. The dynamics of GII.4 RdRp slow down with time in the droplet and leads to the formation of amyloid fibrils (a) FRAP of condensates incubated at 37 °C for indicated time points to measure the dynamics of RdRp molecules in the condensates. **(b)** The recovery graph of the FRAP experiments performed in panel A. The results indicate a slowdown in the dynamics of RdRp molecules over time. **(c)** Negative staining image of RdRp incubated at 37 °C for 12 h. The red arrows indicate the positions of fibrils. **(d)** The kinetics of amyloid fibril formation of RdRp was monitored at 37 °C using ThT fluorescence assay. **(e)** CR absorbance spectra in the absence and presence of RdRp suggests a red shift in the absorbance maxima of CR in the presence of RdRp.

841 **Supplementary Information**

842

843 **Supplementary Table 1**: **Data collection and refinement statistics**

	GII.4 RdRp
Data collection	
Space group	$P2_12_12_1$
Cell dimensions	
a, *b*, *c* (Å)	83.07, 83.70, 90.72
α, β, γ (°)	90. 90, 90
Resolution (Å)	37.21-2.03(2.10-2.03) *
Wavelength (Å)	1.0
R_{sym} or R_{merge}	0.27(7.5)
I / σI	8.4(0.8l)
Completeness (%)	99.86(99.27)
Redundancy	11.4(10.5)
Refinement	
Resolution (Å)	2.03
No. reflections	41484
R_{work} / R_{free}	0.21/0.24
No. atoms	
Protein	3991
Ligand/ion	33
Water	158
B-factors (Å^2)	
Protein	44.09
Ligand/ion	56.32
Water	47.07
R.M.S. deviations	
Bond lengths (Å)	0.005
Bond angles (°)	0.67

844

845 *Values in parentheses are for highest-resolution shell.

846

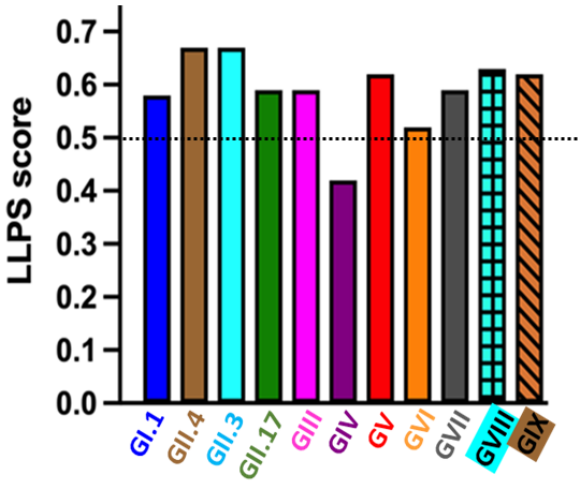

847
848 **Supplementary Figure 1. RdRp of norovirus genogroups has the propensity to form LLPS.**

849 Bioinformatics analysis of the primary amino acid sequences of RdRp of different norovirus

850 genogroups using DeePhase to predict LLPS propensity. The dotted black line indicates the

851 threshold LLPS score of proteins to undergo LLPS.

852